Facultad de Ciencias Físicas
Máster en Astrofísica



Introducción a los estudios bidimensionales de galaxias de baja masa con megara/gtc

Introduction to bidimensional studies of low-mass galaxies with megara/gtc

Por:
María Chillarón Víctor

Tutores:
Jesús Gallego Maestro (UCM)
Cristina Cabello González (UCM)
Nicolás Cardiel López (UCM)

Trabajo de Fin de Máster

Madrid, Junio de 2024

Introduction to bidimensional studies of low-mass galaxies with MEGARA/GTC

Abstract:

The study of galaxy SBS 0335 − 052 W using 2D spectroscopy data from MEGARA (VPH LR-B and LR-R) has provided us with further insights into the galaxy candidate with the lowest measured gas metallicity to date. In this study, data reduction, refined cosmic ray correction of images, and an analysis of the kinematic properties of ionized gas have been carried out. As a result, a spatial structure consisting of two nodes has been obtained, with no discernible kinematic differences. This galaxy exhibits areas of low metallicity and high gas excitation, particularly around the nodes. Its position on the BPT diagram corroborates that the mechanism of gas ionization is the high stellar formation present in the galaxy. The oxygen abundance has been estimated using the N2 and O3N2 tracers (PP04), obtaining, for Region 1, 12+log(O/H)=$7.464^{+0.041}_{-0.047}$ (N2) and 12+log(O/H)=$7.95263^{+0.00066}_{-0.00061}$ (O3N2); and for Region 2, 12+log(O/H) = $7.44^{+0.12}_{-0.17}$ (N2) and 12+log(O/H) = $7.9480^{+0.0012}_{-0.0025}$ (O3N2).

Key words: galaxies: dwarf – galaxies: evolution - galaxies: abundances - galaxies : individual (SBS 0335 − 052), galaxies: kinematics and dynamics - techniques: 2D spectroscopy.

Resumen:

El estudio de la galaxia SBS 0335 − 052 W utilizando datos de espectroscopía 2D de MEGARA (VPH LR-B y LR-R) nos ha proporcionado más información sobre la candidata con la menor metalicidad de gas medida hasta la fecha. En este estudio, se ha llevado a cabo la reducción de los datos, corrección refinada de rayos cósmicos de las imágenes y un análisis de las propiedades cinemáticas del gas ionizado. Como resultados, se ha obtenido una estructura espacial que consta de dos nodos, y que no presentan diferencias cinemáticas. Esta galaxia presenta áreas de baja metalicidad y alta excitación del gas, especialmente alrededor de los nodos. Su posición en el diagrama BPT corrobora que el mecanismo de ionización del gas es la alta formación estelar presente en la galaxia. La abundancia de oxígeno se ha estimado con los trazadores N2 y O3N2 (PP04), obteniendo para la Región 1, 12+log(O/H)=$7.464^{+0.041}_{-0.047}$ (N2) y 12+log(O/H)=$7.95263^{+0.00066}_{-0.00061}$ (O3N2); y para la Región 2, 12+log(O/H) = $7.44^{+0.12}_{-0.17}$ (N2) y 12+log(O/H) = $7.9480^{+0.0012}_{-0.0025}$ (O3N2).

Palabras clave: galaxias: enana – galaxias: evolución - galaxias: abundancias - galaxias : individual (SBS 0335 − 052), galaxias: cinemática y dinámica - técnicas: espectroscopía 2D.

Contents

1. Introduction **3**
- 1.1. Why are local low-mass galaxies of interest? . . . 3
- 1.2. SBS 0335−052 W: the lowest-metallicity emission-line galaxy known. . . . 4
- 1.3. Environment of the SBS 0335−052 system and evolution . . . 4

2. MEGARA instrument and Dwarfs4MOSAIC ITP **6**
- 2.1. MEGARA . . . 6
- 2.2. International Time Programme (ITP): Dwarfs4MOSAIC . . . 6

3. MEGARA Data Reduction Pipeline and refined cosmic ray cleaning **7**
- 3.1. MEGARA Data Reduction Pipeline . . . 7
- 3.2. Refined cosmic rays cleaning . . . 9

4. Study of SBS 0335 − 052 W **10**
- 4.1. Spectra lines identification . . . 10
- 4.2. Analysis of final Row Stacked Spectra (RSS) . . . 11
- 4.3. Line-ratios maps . . . 14
- 4.4. BPT diagram . . . 17
- 4.5. 12 + log(O/H) metallicity . . . 18
  - 4.5.1. The N2 index . . . 18
  - 4.5.2. The O3N2 index . . . 18

5. Summary and conclusions **22**

6. Future work **23**

Bibliography **24**

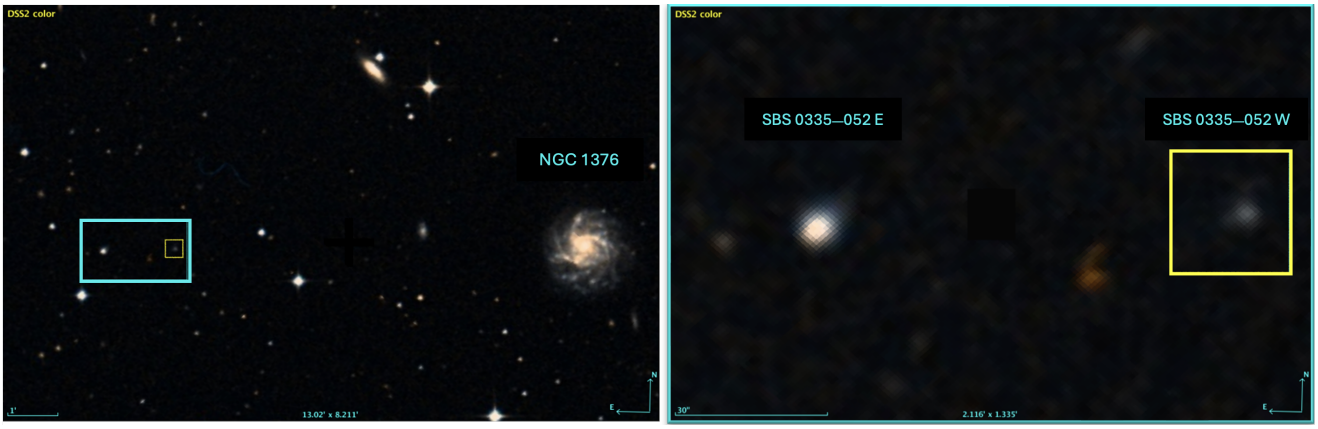


Figure 1: *Left panel*: Environment of the SBS 0335 − 052 system and NGC 1376. The blue box contains both SBS 0335 − 052 E and W (Size: 13.02' × 8.211'). *Right panel*: Zoom of the SBS 0335 − 052 system from the previous image. Now the blue box surrounds our galaxy: SBS 0335 − 052 W (Size: 2.116' × 1.335'). Orientation: North is up and east is to the left. Images from Aladin.

1. Introduction

One of the open questions in Astrophysics and Cosmology is how the formation and evolution of the first galaxies occurred. We aim to understand the characteristics of these sources that emitted the first light in the Universe, bringing an end to the dark age and initiating the Epoch of Reionization.

The Universe became neutral after Recombination at z∼1100, and remained so until the highly energetic photons emitted by Population III stars began to create bubbles of ionized gas. These bubbles eventually grew and overlapped with the birth of the first galaxies (Wise 2019). Consequently, the neutral intergalactic medium (IGM) that made up the Universe became reionized into a plasma again. Both theoretical models and observations (Fan et al. 2006) suggest that the reionization period occurred at redshifts between 6 and 20, though this remains a subject of debate.

To trigger reionization, we need two fundamental ingredients, as explained by Kimm et al. (2017): star formation and escaping LyC photons (photons with a wavelength lower than 912 Å, as energies above 13.6 eV are required to ionize neutral hydrogen). Their study suggests that reionization is likely driven by dwarf galaxies (Atek et al. 2024) and we will be analyzing one local counterpart of them in this study.

1.1. Why are local low-mass galaxies of interest?

To study the epoch of Reionization, we would ideally search for the first galaxies in the Universe and extract information directly from them. Nevertheless, observing the first galaxies at high redshift (z ∼ 6 - 10) is not easy due to their faintness and compact size. Therefore, the best approach we can take involves searching for local galaxies exhibiting similar behavior that can serve as counterparts to those from the reionization epoch instead (Thuan et al. 1997).

Among the requirements that local analogs should meet, we seek low-mass galaxies with low metallicity and high SFR. Some authors like Thuan et al. (1997) refer to them as 'primeval galaxies' and define them as 'young systems undergoing their first major burst of star formation'. Other authors discuss 'Extreme Metal-Deficient' (XMD) galaxies (Izotov et al. 2024), which also add criteria such as low luminosity and high specific star formation rate. Specifically, they constrain the oxygen abundance 12 + log(O/H) in the range ∼ 6.9–7.1. The study by Herenz et al. (2023) directly points to 'Blue Compact Dwarf' (BCD) galaxies (de Paz et al. 2003) as galaxies that possess the necessary characteristics to be analogs of those from the reionization epoch.

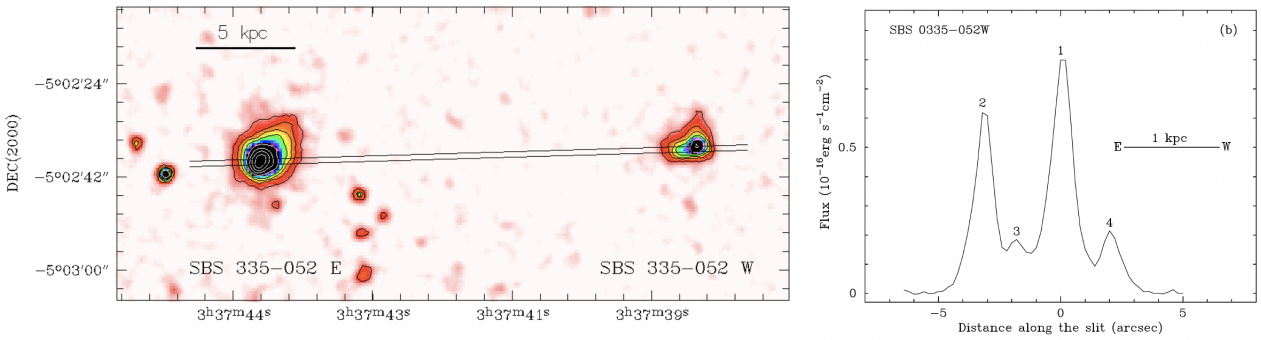


Figure 2: *Left*: figure 1 from Izotov et al. (2009), in which we can see the location of the slit for their spectroscopic study over a 2.2 m Calar Alto telescope B image of the galaxy system SBS 0335 − 052 E and SBS 0335 − 052 W. *Right:* figure 2 from Izotov et al. (2009), Hβ flux distribution along the slit shown on the left, where the four regions of SBS 0335 − 052 W are distinguished.

Region No.	1	2	3	4
12 + log(O/H)	7.22 ± 0.07	7.01 ± 0.07	6.98 ± 0.06	6.86 ± 0.14

Table 1: Oxygen abundances of the four regions of SBS 0335 − 052 W measured by Izotov et al. (2009) shown in figure 2.

1.2. SBS 0335−052 W: the lowest-metallicity emission-line galaxy known.

The galaxy of this study is SBS 0335 − 052 W (J2000 RA $03^h37^m44.06^s$ DEC −05° 02' 40.2" [1]), the second member of the SBS 0335 − 052 system located at redshift 0.013392 ± 0.000006 (d = 54 Mpc) (Filho et al. (2013), NED). It is a system composed of a pair of extremely metal-deficient star-forming dwarf galaxies separated by 22 kpc in projection (see figure 1) (Herenz et al. 2017). The companion galaxy is SBS 0335 − 052 E, which was the first to be discovered and has been extensively studied for over 20 years. (Thuan et al. (1997), Izotov et al. (2009),Wofford et al. (2021), Herenz et al. (2023)).

SBS 0335 − 052 W was first discovered by Pustilnik et al. (1997), based on observations of the 21 cm line of neutral hydrogen cloud in which the system is embedded. In this cloud, whose dimensions are 66 × 22 kpc and it is elongated in the east-west direction, they observed two distinct, slightly resolved HI peaks positioned nearly equidistant from the center of the HI cloud, with a separation of about 28 kpc. With the measurement of their heliocentric velocities, they unequivocally determined that both SBS 0335 − 052 E and W belonged to a single system.

Among its spectroscopic studies, the first was a 6-m telescope spectrum by Pustilnik et al. (1997), which revealed emissions of Hβ, [OIII]λ5007, and Hα, resulting in a redshift similar to SBS 0335 − 052 E. VLT/FORS+UVES long-slit spectroscopy carried out by Izotov et al. (2009) provided extensive information about its structure and composition (see Fig. 2). On the one hand, they identified four regions where they measured the oxygen abundance (shown in table 1), which represent the lowest oxygen abundances ever derived in emission-line galaxies, supporting previous conclusions that SBS 0335 − 052 W is the lowest-metallicity emission-line galaxy known. Other studies in the X-ray range indicate that the galaxy SBS 0335 − 052 W is brighter than its companion, SBS 0335 − 052 E, due to X-ray binaries (Thuan et al. 2004).

1.3. Environment of the SBS 0335−052 system and evolution

Numerous studies have attempted to provide insights into the evolution of the system, which is embedded in an HI halo featuring elongated tidal tails extending to the east and west, along with a faint diffuse bridge linking the two galaxies (Ekta et al. 2009). In doing so, we must consider the presence of the large-scale spiral galaxy NGC 1376, located at a distance of 150 kpc from the system (Pustilnik et al. (2001)), with a redshift of 0.013937 (V = 4149.2 km/s). It is worth noting that

[1] SIMBAD database, SBSG 0335-052 – Blue Compact Galaxy

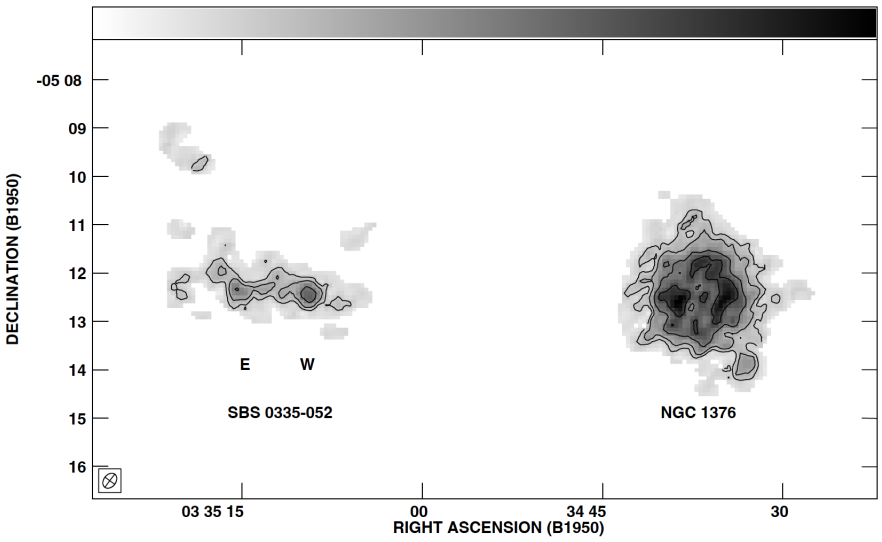


Figure 3: HI map of the SBS 0335 − 052 system and the companion galaxy NGC 1376 from Pustilnik et al. (2001). The gray scale is a linear representation of HI surface density ranging from 0 (white) to 16×10^{20} cm^{-2}. The ellipse in the lower left corner indicates the beam size.

NGC 1376 and the system are aligned in the east-west direction, raising suspicions of interaction between them.

The initial studies by Pustilnik et al. (1997) propose that the galaxies SBS 0335 − 052 E and W are two young objects of the same age within a massive HI cloud. Alternatively, if the metallicity of SBS 0335 − 052 W suggests it is older, then it would be encountering the pristine neutral gas cloud, leading to collapse in the eastern part of the cloud and the formation of SBS 0335 − 052 E.

A few years earlier, Elmegreen & Elmegreen (1987) had classified NGC 1376 as a spiral 'whose arms are fragmented spiral pieces with no regular pattern'. This suggests that the spiral had recently experienced a tidal disturbance, and the HI map pointed to the small galaxies in the southwest. Four years after the discovery, Pustilnik et al. (2001) found the presence of tidal tails at the end of the system, supporting the notion that tidal interactions triggered star formation, either by NGC 1376 or by the gravitational interaction of the two HI clouds (see HI map from Pustilnik et al. (2001) in Fig. 3).

According to Thompson et al. (2006), who also support this scenario, in most merger simulations, significant star formation occurs after the first encounter, which would suggest the possibility that the SBS galaxies have already had a first encounter with NGC 1376 and have been close in the past. As stated by Thompson et al. (2009), it is possible that SBS 0335 − 052 W and E are in the process of a minor merger with NGC 1376.

In the following sections, we present the study of the galaxy SBS 0335 − 052 W based on integral field spectroscopy observations from MEGARA. Section 2 describes the instrument and the observation program. Section 3 focuses on data reduction and refined cosmic ray cleaning; section 4 describes the analysis of the products to obtain metallicity, gas ionization and derived property maps. Finally, we present our conclusions and future work for SBS 0335 − 052 W in the last sections.

VPH Name	Setup	R_{FWHM}	$\lambda_1 - \lambda_2$ (Å)	λ_c (Å)	$\Delta\lambda$ (Å)	Δv (km/s)	CDELT1 (Å)	CRVAL1 (Å)
VPH480-LR	LR-B	6059	4332 - 5196	4800	0.792	49	0.23	4280
VPH675-LR	LR-R	6099	6094 - 7300	6747	1.106	49	0.31	6030

Table 2: Scientific requirements of MEGARA VPHs used in this study. For a complete overview of all 18 VPHs check out MEGARA Cookbook (Castillo-Morales et al. 2020).

2. MEGARA instrument and Dwarfs4MOSAIC ITP

2.1. MEGARA

All data of the galaxy SBS 0335 − 052 W have been taken with MEGARA (Multi-Espectrógrafo en GTC de Alta Resolución para Astronomía, Gil de Paz et al. (2015)). MEGARA is a spectrograph based on fibers for both Integral-Field Unit (IFU) and Multi-Object Spectrograph (MOS) modes. MEGARA focal plane component is attached to the Folded-Cassegrain F (FC-F) focal station of GTC, with optical fibers that lead the light to the spectrograph at GTC Nasmyth A platform (Gil de Paz et al. 2016). It has been commissioning at the 10.4m GTC (Gran Telescopio Canarias) since 2017. Our data have been taken using the MEGARA IFU which is called Large Compact Bundle (LCB). The field covered is 12.5" × 11.3" in size and uses 567 hexagonal spaxels of 0.62" along with 56 sky spaxels of equal size distributed in 8 bundles of 7 fibers around the outskirts of the field at about 2' from the center of the LCB (MEGARA Cookbook (Castillo-Morales et al. 2020)).

MEGARA is equipped with a set of Volume-Phase Holographic (VPH) disperser elements, which are called low(LR), mid(MR), and high-resolution(HR) VPHs in the 3700 − 9700Å range, $R \sim 5000$, 12000 and 20000 respectively. In this study, we are working with LR-B and LR-R whose characteristics are displayed in table 2. The last two columns also indicate the reciprocal (linear) dispersion (CDELT1) and wavelength for the initial pixel (CRVAL1 for CRPIX=1), which will be useful to convert our spectra from pixels to wavelength.

2.2. International Time Programme (ITP): Dwarfs4MOSAIC

The observations of this galaxy are part of La Palma International Time Programme (ITP) *'Dwarfs4MOSAIC: A 2D study of low-mass star-forming galaxies as low-redshift analogs to reionization-epoch primeval galaxies: A pilot study for MOSAIC at ELT'* whose Principal Researcher is Jesús Gallego (Universidad Complutense de Madrid) and of which 58 researchers from 26 different institutions are members, including Cristina Cabello and Nicolás Cardiel.

MOSAIC (Multi-Object Spectrograph for Astrophysics, Intergalactic medium studies and Cosmology) will be a first generation spectrograph for the future ESO 39m Extremely Large Telescope (ELT), whose first light is currently planned for 2032.

The project of this ITP focuses on obtaining two-dimensional (2D) spatially resolved high spectral resolution Integral Field Spectroscopy of low-mass star-forming galaxies at the local universe, that behave as counterpats of primeval galaxies. Specifically, MEGARA has 60 dark night hours and 20 grey night hours and will observe 19 galaxies with a single pointing per object, using three VPHs (LR-R, -B, and -U) to cover the main emission lines in the observed wavelength range. The aim is to study their physical and kinematic properties to shed light on the epoch of reionization and the role that lowmass galaxies played. Finally, these studies will contribute to create a reference galaxy sample to test strategies and models for MOSAIC.

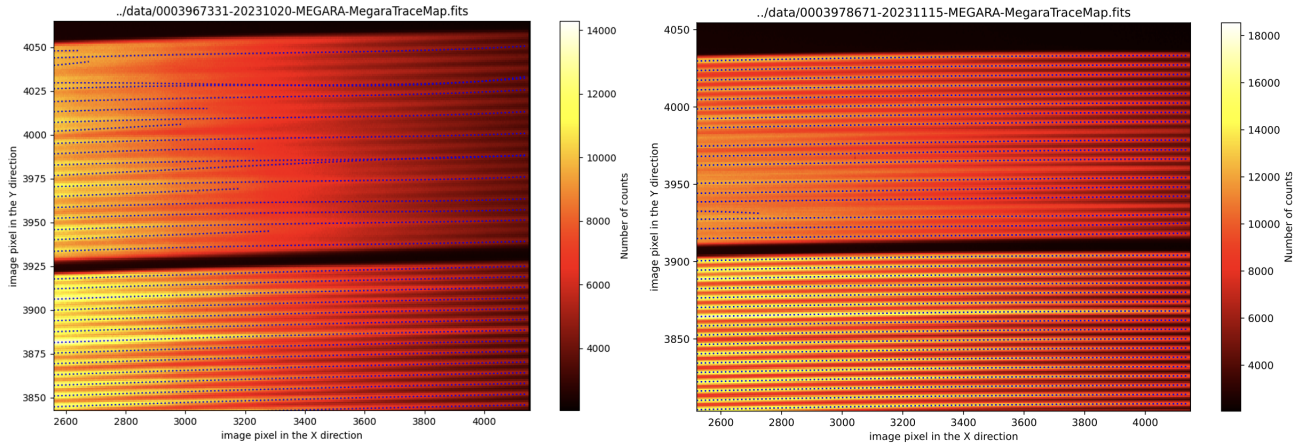


Figure 4: Traces of the fibers from the master_traces.json file overplotted on two flat images. These sections correspond to the upper right corner of the images, where it has been noted that there is incomplete tracing. On the left is LR-B, where the loss of fiber trace and blurring are more evident. On the right is LR-R, where only 3 fibers could not be traced.

3. MEGARA Data Reduction Pipeline and refined cosmic ray cleaning

For the analysis of SBS 0335 − 052 W, we combine images from two VPHs: LR-B and LR-R. The data were taken on October 20th and November 15th 2023, respectively. Both nights were dark, being the observing conditions photometric throughout them. During the observation, the seeing for LR-B and LR-R were 0.9" and 0.8". Three exposures of 1200 seconds each were taken for each VPH (3×1200s).

It is worth noting that there is a slight offset between the pointings for each VPH, centered at (RA = 03:37:38.317, DEC = −05:02:37.502) for LR-B and at (03:37:38.315, −05:02:37.502) for LR-R. Therefore, the same region of the galaxy will not fall on the same spaxel when comparing both VPHs.

Data have been reduced using version 0.14.1 of megaradrp. The entire process can be completed following the instructions of the MEGARA Cookbook (Castillo-Morales et al. 2020) and MEGARA DRP Documentation.

3.1. MEGARA Data Reduction Pipeline

The MEGARA Data Reduction Pipeline enables the processing of the images delivered by the telescope to the user, converting them into scientific images from which valuable information can be extracted. It was developed in Python and consists of 8 steps that carry out bias correction, trimming, fiber tracing, wavelength calibration, fiber-flat and twilight-flat correction, sky substraction and absolute flux calibration whenever possible.

- **Step 0: Bias Image**. In MEGARA, light is detected using a Charge-Coupled Device (CCD), that adds effects to the images that need to be removed. Among these effects, we deal with a pedestal level, called bias, that is added before the conversion to ADUs (Analog-to-Digital Units) in order to avoid a negative or null signal.

  We need bias images from the telescope which are taking with no integration time. In our case, the CCD is read by two amplifiers so the bias is different in the upper and lower parts of an image.

  It is also important to correct from pixels which are no longer working, usually called dead or hot pixels, using a Bad-pixels Mask that must be provided. In MEGARA, we do not correct from dark current because the rate of spontaneous electrons created due to the detector temperature is insignificant, and the same happens with pixel-to-pixel variations in sensitivity.

  The product is a MasterBias image that will allow us to subtract the bias signal in the following steps.

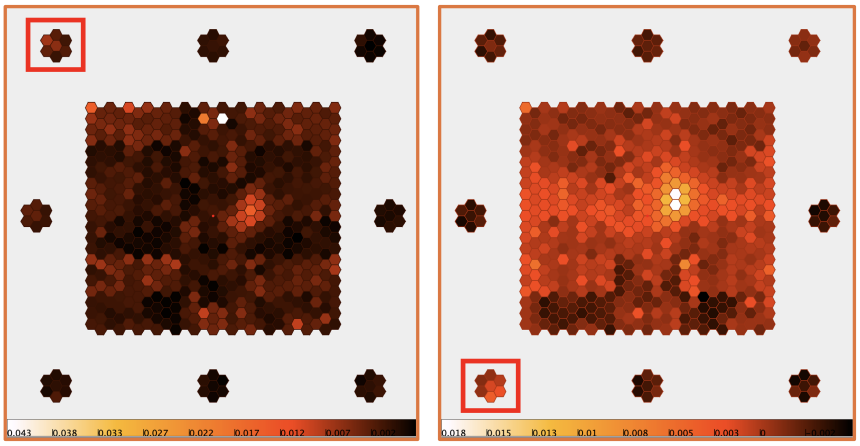


Figure 5: White light images of SBS 0335 − 052 W for LR-B (left panel) and LR-R (right panel). The sky bundles ignored in the final step of the pipeline are indicated within the red boxes: bundle 93 (left) and 96 (right). Images from MEGARA QLA software.

- **Step 1: Trace Map.** In order to extract the flux of each fiber from the detector, we need to know the path they describe on it. Finding these positions is what we call "tracing the fibers". For this step, we need fiber-flats which are images that are taken illuminating the focal plane with a continuum lamp. The pipeline uses information from the instrument configuration to identify each fiber and match it with its trace.

  Finally, the product is a `master_traces.json` image that we can visualize over a raw or processed image. This figure allows us to detect a bad tracing of the fibers, which has occurred in both VPHs in the upper right corner of the detector (see Figure 4). A reason that may explain this blurring could be that some fibers have become misaligned over time and their light is not well focused. Recently, in May 2024, it has been confirmed that the clarity of the traces depends on temperature, and it is important to perform calibrations at a temperature similar to that during observation, to avoid the effects of telescope heating.

  Thanks to this discovered feature during our study, a new tool, Fixing defective traces in megaradrp, is available with the megaradrp. If a trace is still visible but the program cannot measure its intensity peak, it will stop tracing. However, we can manually recover it, and this is what can be done with the new tool. The problem arises when the trace becomes blurred or has gaps, in which we cannot trace the fiber. The reason why it was not used for our galaxy is that the poorly traced or missing fibers do not belong to spaxels that are part of the nodes or structure of interest in the galaxy.

- **Step 2: Model Map.** Similar to Trace Map step (uses flat images and the results are used to extract flux from fibers) but it is used for an advanced extraction. The fibers are found using the `master_traces.json` image and then, their light profiles are modelled from vertical cuts of the image.

  This step has not been implemented in our study, because the tracing is successfully done with the previous step.

- **Step 3. Wavelength Calibration**. To understand the fibers spectra, it is essential to find the wavelength solution for each fiber. To do this, we use arc-lamp images whose lines are well known and will be used to match the peaks we see with a Lines Catalog. The arc-lamp images are processed, and the flux is extracted making sure we check out the offset before overlapping the traces.

  The result is a `master_wlcalib.json` file that contains the information of the fitted polynomials of the wavelength solution.

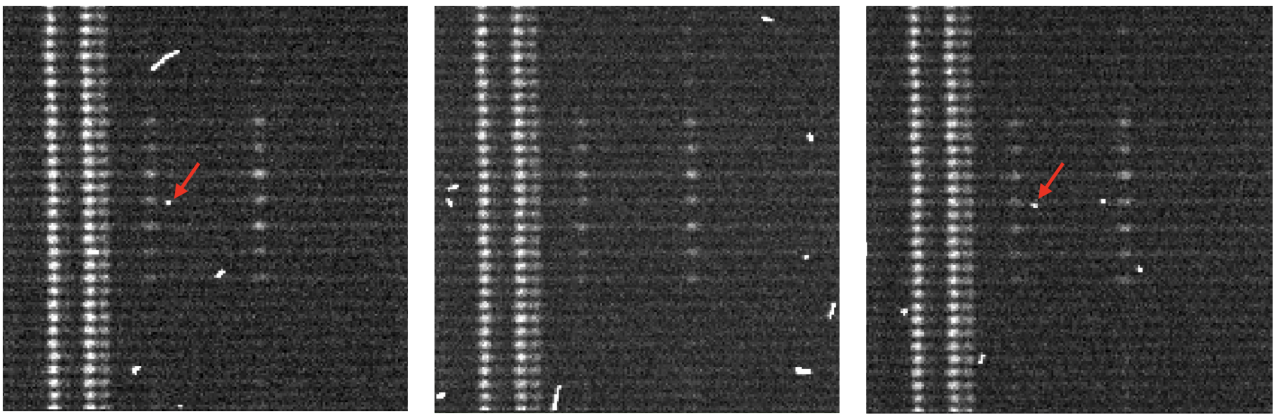


Figure 6: Raw images of the object showing the region around the pixels affected by cosmic rays in fiber 329 from LR-R. The red arrow indicates the removed cosmic rays which have affected two of the three images in the same pixels.

- **Step 4. Flat Field Correction**. Each fiber has a different optical transmission compared to the others, so we need to correct from this using fiber-flat images. The normalization of the product, `master_fiberflat.fits`, is done using a fitted spline of the average of all fibers.
- **Step 5. Illumination correction**. Twilight images are useful to correct changes of the global illumination of the field of view since there are differences between observing the object in the sky and taking fiber-flat images. With twilight images we can assume that the field is uniformly illuminated.

  In this case, twilight images have not been provided by the telescope so we have skipped this step.
- **Step 6. Flux calibration**. Observations of spectrophotometric stars are needed for absolute- or relative- flux correction (depending on weather conditions). This step extracts the star spectra and finds its centroid in the field of view. This offset is used to find the spaxels whose signal will be summed to get the star flux.
- **Step 7. LCB IFU Scientific observation**. The object images are reduced using the calibration results from previous steps. Furthermore, we have the option to exclude those sky bundles that may be contaminated with light from other objects.

The images resulting from the data reduction are Row-Stacked Spectra (RSS), consisting of the stacked spectra of all 623 fibers. In figure 5, the White Light images of SBS 0335 − 052 W for LR-B and LR-R are displayed surrounded by the eight sky bundles, the red squares mark the ignored ones.

3.2. Refined cosmic rays cleaning

A preliminary step before analyzing the fiber spectra (line identification, maps or line ratios) is the elimination of cosmic rays (CR). During exposure time, numerous cosmic rays with a random pattern reach the detector, most of which will disappear by the median of the 3 images in the reduction pipeline. However, some residual cosmic rays have persisted through this image combination because the affected pixels coincide in at least two images.

At this point, a second-iteration cleaning of the images from cosmic rays is required. Ideally, it should be performed on raw images that would undergo the reduction process again to obtain a cosmic ray-free product. As a stopgap solution, we have cleaned the final RSS of each VPH, and specifically, cosmic rays near emission lines. Figure 6 shows an example of residual cosmic rays that have affected the same pixels from two of the three raw images of the object in fiber 329 of LR-R.

The `Cosmic_rays_cleaning` code implemented in Python removes the signal of a cosmic ray by linearly interpolating the continuum aside. From the `final_rss.fits` image, fiber id and pixels

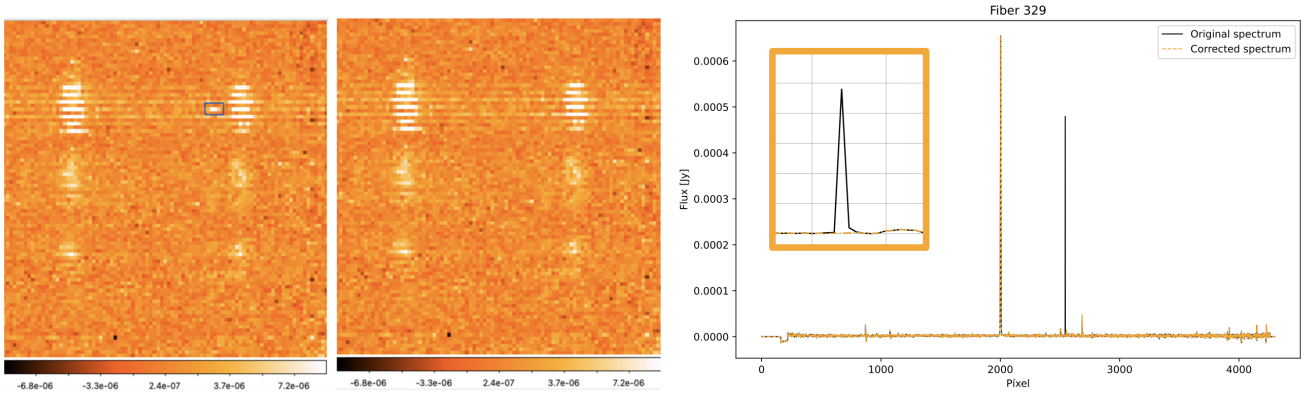


Figure 7: Fiber 329 from LR-R affected by a cosmic ray near the [SII] lines. Visualization of the before and after on the RSS image with DS9 (left panel), and overlay of the initial and corrected spectra of this fiber (right). A zoom of the linear interpolation of the cosmic ray is shown in the orange box.

affected by the cosmic ray as arguments of the function, it generates an identical spectrum free of the defect and replaces it in the position of the affected fiber. Figure 7 shows the result of refining the cleaning of CR for fiber 329 in LR-R.

This cosmic ray cleaning is crucial because it would affect the analysis of galaxy properties, such as line ratio maps (this is exactly how their presence was detected, as they produced such a high signal level that resulted in blank spaxels in the node area). It makes us consider that if many residual cosmic rays have persisted for our galaxy after the reduction pipeline, the combination of images carried out during the process will not be sufficient, and an additional intermediate step will be needed. This new solution should be automatic and, for instance, it could consist of creating a mask with those pixels affected by cosmic rays in an image, and then perform an intersection to discover if any of them survive for every image taken.

4. Study of SBS $0335-052$ W

4.1. Spectra lines identification

The abundance of elements present in the ionized gas of the galaxy and their ratios will shed light on chemical enrichment, metallicity, and evolution. The first step is to identify spectral lines of interest. For this, the NIST Atomic Spectra database was used, and the spectrum of the brightest spaxel of each VPH was analyzed. Figure 8 shows the main emission lines found in these spectra:

- **LR-B**: Hγ, [OIII]λ4363, HeIλ4471, Hβ, [OIII]λ4959 and [OIII]λ5007.
- **LR-R**: [OI]λ6300, Hα, [NII]λ6584, HeIλ6678, [SII]λ6717, [SII]λ6731 and HeIλ7065.

A first result for the galaxy SBS $0335-052$ W can be obtained from this line identification. If we know the rest-frame wavelengths and the observed ones from their spectra, we can estimate the redshift according to

$$\lambda_{\rm obs} = \lambda_{\rm rf}(1+z). \tag{1}$$

From the emission lines in LR-B, their individual redshifts have been calculated, with a mean of 0.013353 and a standard deviation of 0.000010. And for the LR-R, the mean redshift is 0.013379 with a standard deviation of 0.000023. Taking into account the range of variation of the data, the last one is consistent with the value measured by (Filho et al. (2013), NED) from HI emission, 0.013392 ± 0.000006. In regard to the measured redshifts, which should be similar, we will assess their compatibility by examining their difference relative to the standard deviation. The absolute difference of the means

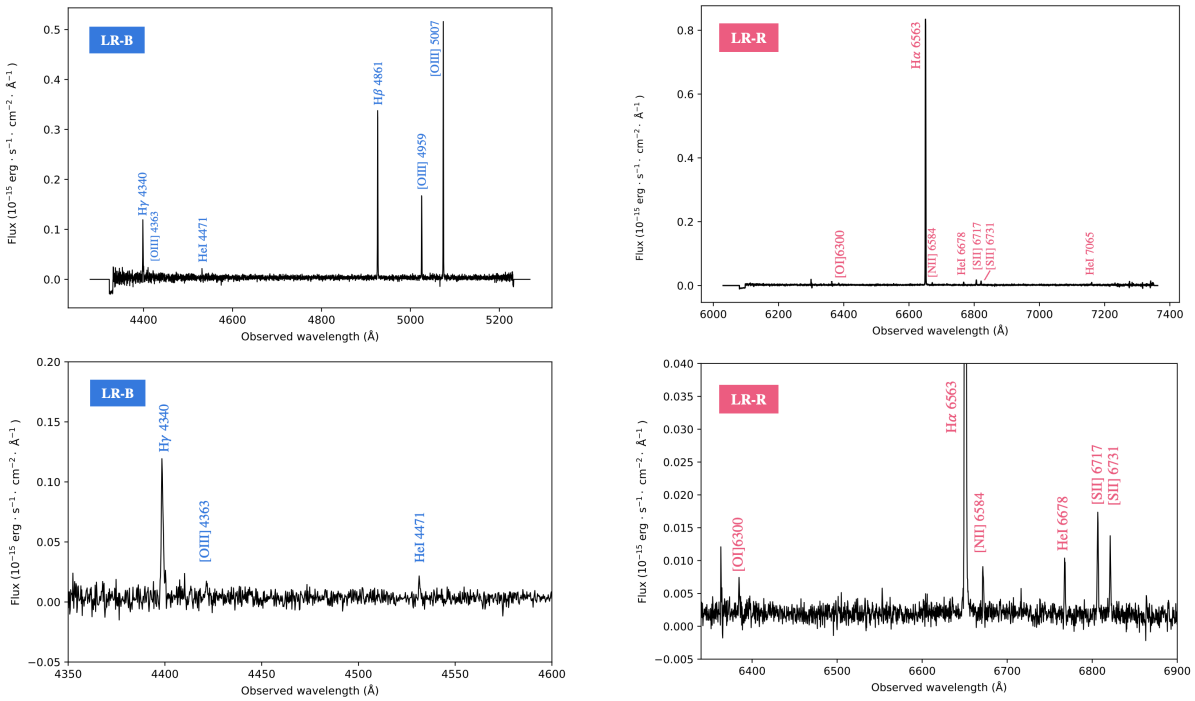


Figure 8: Identification of the lines on the spectrum of the brightest spaxel for LR-B (spaxel 222) and LR-R (spaxel 331). In the bottom row, weaker lines have been magnified to visualize and distinguish them from the continuum.

divided by the quadratic sum of the standard deviations results in 1.04 times sigma (standard deviation). Since this is less than two, both redshifts fall within a 2σ effect and are therefore consistent measurements.

4.2. Analysis of final Row Stacked Spectra (RSS)

As part of the analysis of the reduction products, visualizing property maps of SBS 0335 − 052 W is essential. These maps (flux, line-of-sight radial velocities, velocity dispersion, ...) provide us with information about the spatial structure of the galaxy, for instance if there are different nodes or regions, and about kinematics. In order to obtain them, we use version 0.1.1 of *megara-tools* software developed by MEGARA team. In particular, we perform the analysis of spectra from the final RSS using 'megaratools-analyze_rss' tool.

The aim of this tool is to fit emission lines of all 623 fibers spectra. To do this, we need to specify the fitting method (0=Gauss-Hermite, 1=simple Gaussian, 2=double Gaussian), the SN ratio, the galaxy redshift, and we will also set the wavelengths for the line fit, the continuum fit, and those we would like to exclude. The output of this tool is a FITS file that contains the same number of rows as the final RSS used and 29 columns (one per derived property). It is important to point out that the channel numbering provided by the MEGARA Cookbook is offset by 1 unit in index, relative to the `-c` command at the execution instruction of the tool. That is, if velocity corresponds to channel 16 according to the Cookbook, the tool instruction must select column 17 from the FITS file. A PDF file is also generated, containing the visualization of all the line fits performed on the 623 fibers.

For this study, we have used method 1 and a SNR of 5. The choice between methods 0 and 1 depends more on the signal-to-noise ratio, being Gauss-Hermite suitable when signal is high enough. Opting for the Gaussian method guarantees robust results even if the signal is fainter.

During the creation of the maps with `megaradrp.visualization`, we found out that, by default, the plot size adjusted to the envelope of the spaxels with signal in the map. To change this and have all plots display the complete field of view, we needed to uncomment lines 372 and 373 in the `visualization.py` file. Another aspect to improve lies in the velocity calculation, where initially,

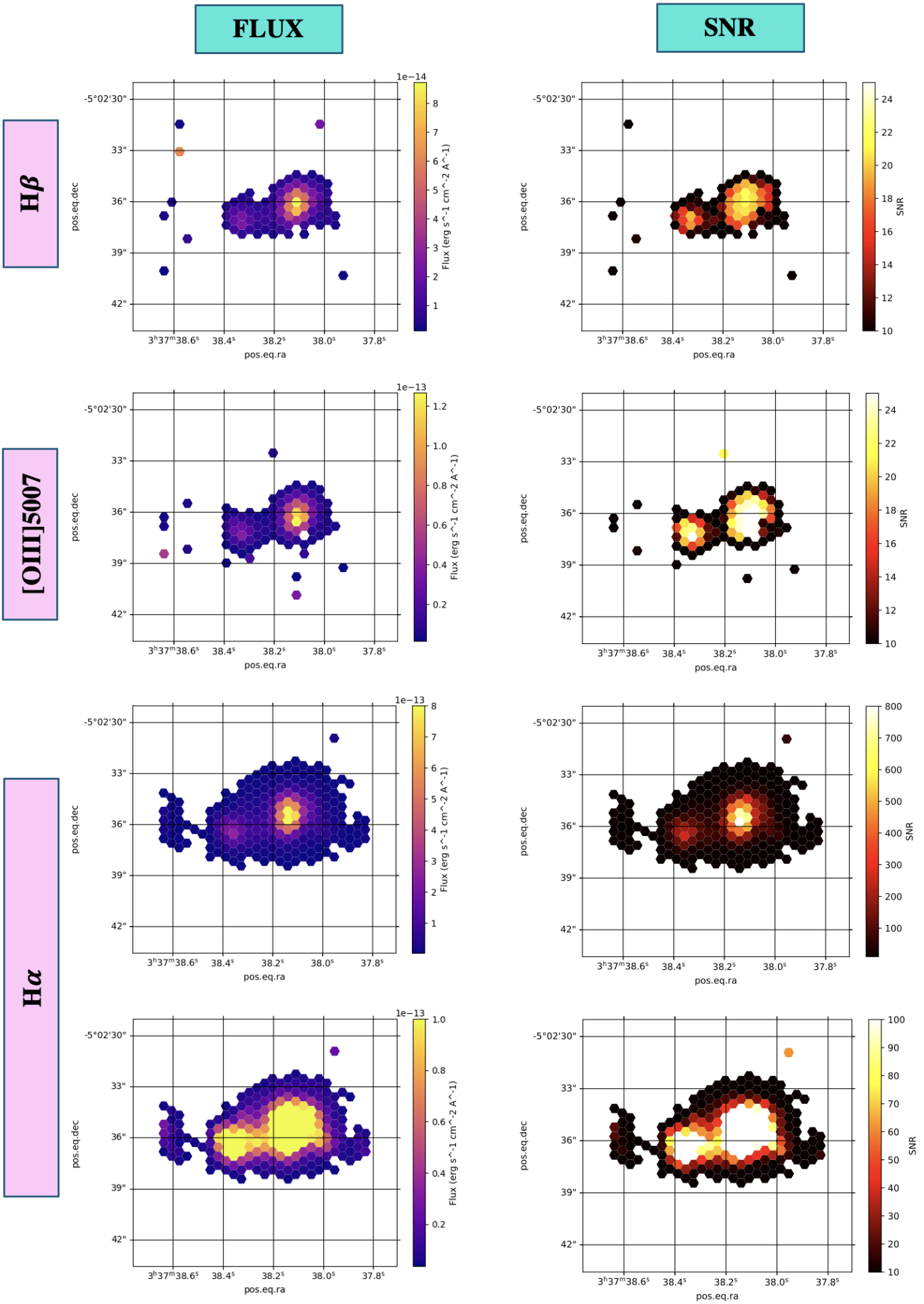


Figure 9: Maps of derived properties: Flux (channel 6) and SNR (channel 3) of Hβ, [OIII]5007 and Hα. Fitting method used 'Simple Gaussian', SNR value of 5. For the Hα line, flux and SNR maps are presented with two different settings for `--max-cut` (scale of color bar). This allows us to visualize the maximum flux and SNR of the brightest spaxels, and with the second setting, we can study a lower threshold.

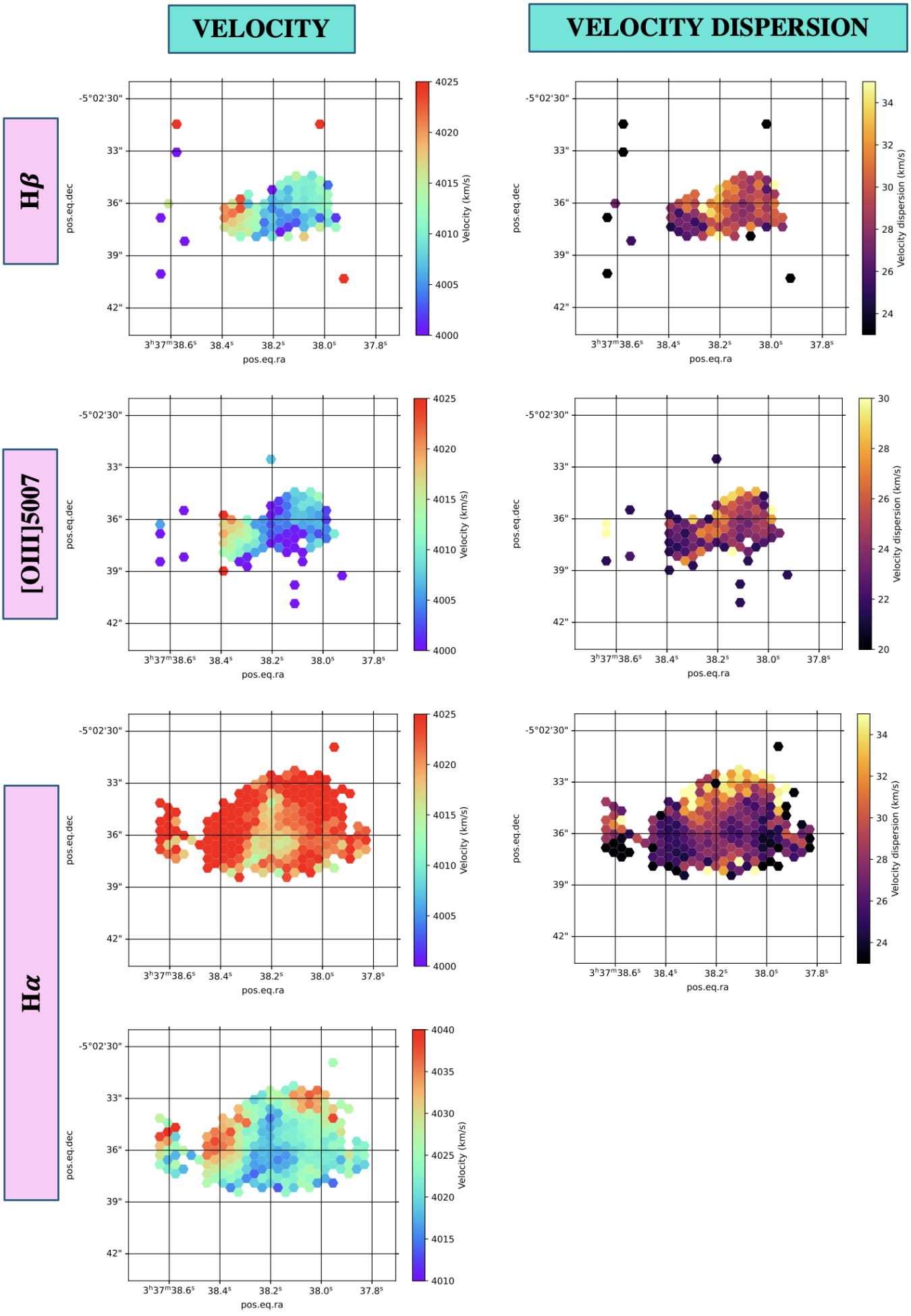


Figure 10: Maps of derived properties: Velocity (channel 16) and velocity dispersion (channel 17) of Hβ, [OIII]5007 and Hα. Fitting method used 'Simple Gaussian', SNR value of 5. For the Hα line, there are two maps with different settings for `--max-cut` and `--min-cut` (scale of color bar).

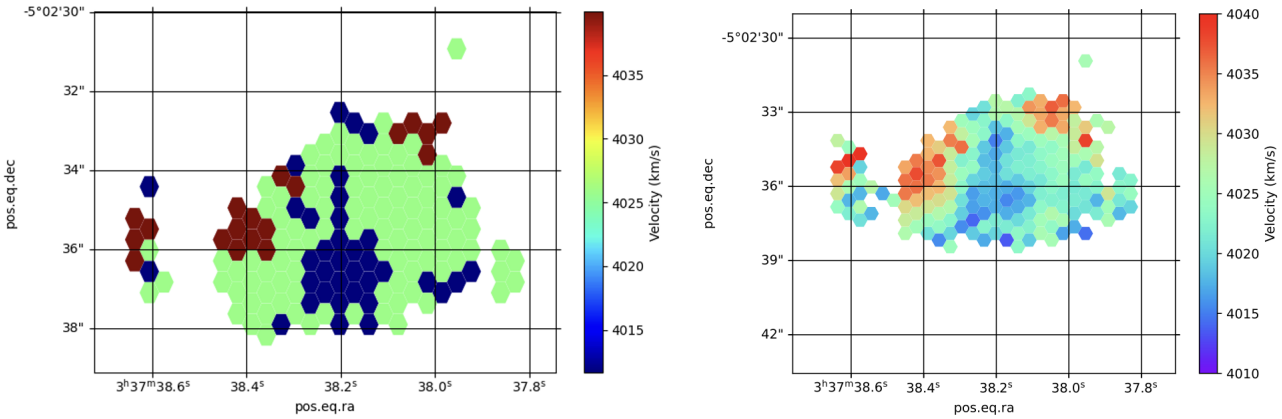


Figure 11: The images display two velocity maps calculated from the Hα line for SNR=5. On the left, we have the map obtained before (1) adjusting the plot size to the total field of view and (2) introducing data normalization by the maximum to avoid calculation error resulting in discrete values. On the right, the velocity map with the corrections applied.

identical discrete values were obtained for sets of spaxels (see Figure 11). This was resolved by modifying the Python code of `analyze_rss.py`, adding `rss/= np.max(rss)` after the line in which rss is defined, as it is a numerical issue.

Figures 9 and 10 show the property maps derived from the three most intense emission lines: Hβ, [OIII]λ5007, and Hα.

- **Flux** maps of the three lines show a two-node spatial structure. The brightest node, henceforth called 'Region 1', corresponds to node 1 detected by Izotov et al. (2009); while the second node, to the left, matches node 2 from their study ('Region 2').

  As for nodes 3 and 4 that they detect, we do not observe them because the seeing on the night of observation (0.8"/0.9") is greater than the spaxel size (0.62"), causing the signal to spread out and blur. MEGARA was designed for the seeing conditions of La Palma in the 1990s, but these have degraded since then.

- **SNR** maps indicate how high signal is relative to noise; the most intense signal is exactly located over the nodal zone. Specifically, for Hα we present two SNR maps: the first one shows the high SNR achieved at the brightest spaxel, over 800. The second map aims to analyze the SNR value in those spaxels that were below 100 in the previous map. These maps show a measurement of the quality of the observations.

- **Velocity and velocity dispersion**. Velocity maps also reinforce the separation of the two mentioned nodes. Gas over both nodes has a higher velocity than in the internodal region. If we look at the second node, we see that the upper part is redshifted while the lower part is blueshifted. This could indicate that the node is rotating or that it is an expanding gas bubble. On the other hand, values of the velocity dispersion does not accentuate any special gas pattern in the galaxy. The only notable point is that Node 2 has lower values, which could be due to (1) being less massive, (2) being less turbulent, or (3) both.

4.3. Line-ratios maps

Line ratios are a key tool in analyzing gas ionization or dust content. We use the study of Arroyo-Polonio et al. (2023) on Green Peas as reference, which provides us with the most interesting line ratios for low-mass galaxies like SBS 0335 − 052 W. In our case, we will only combine emission lines close enough in wavelength to reduce the effects of extinction (figure 13).

- The first map shows the relationship between **N2** $\equiv$ **[NII]λ6584/Hα**, this ratio traces low metallicity zones and regions with gas excitation according to Pettini & Pagel (2004). In their

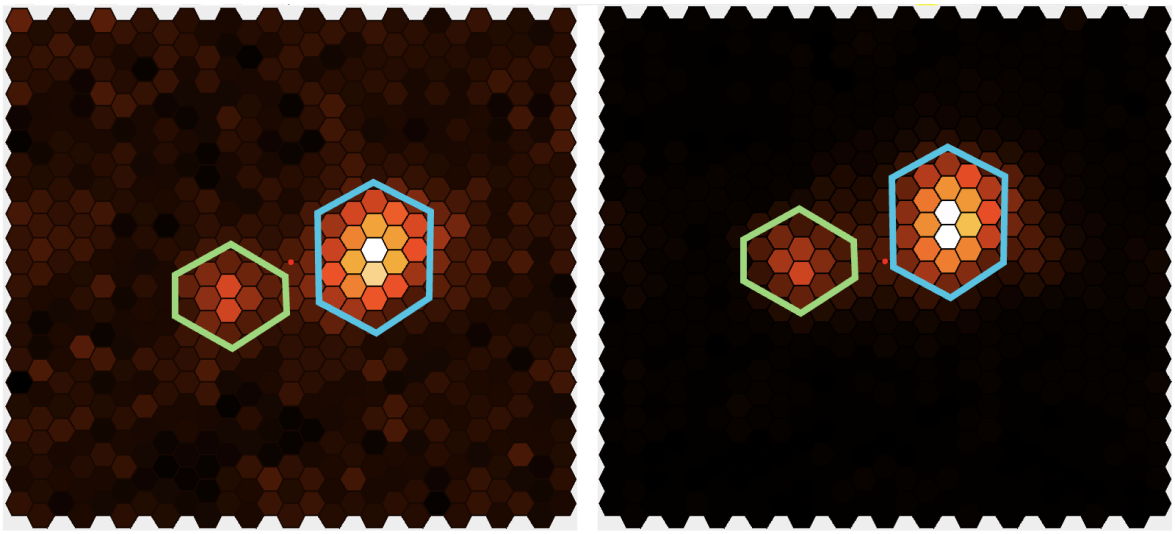


Figure 12: Selected spaxels for regions 1 (blue) and 2 (green) over the nodes of the galaxy in the LR-B (left, background image represents Hβ flux) and LR-R (right, background image represents Hα flux) VPHs for the BPT diagram.

study, depending on the N2 range of values, they provide a linear equation to aproximate the abundance of O (N2 $\sim(-1.8, 0.8)$); and a third order polynomial for $2.5 < \text{N2} < 0.3$ (equation 2). We will calculate oxygen abundance in the following sections of this study.

- **[OI]λ6300/Hα** ratio peaks in the ionization fronts of galaxies. Along with **[SII]λ6716+6731/Hα**, they trace the opacity of the gas column. Paswan et al. (2022) determine that having low values for both ratios represents a thin column of gas (and a high gas excitation) since LyC photons can escape this way. Qualitatively, we observe that the areas with the lowest coefficients for both ratios coincide on the maps. They are mainly located in Region 1, also coinciding with the spaxels with the lowest N2.

- **[SII]λ6716/[SII]λ6731** is a useful ratio to determine electron density. Higher values of it indicate low electron density (Pérez-Montero 2017). The value of this coefficient for SBS 0335 − 052 W is slightly lower in the nodal regions of the galaxy.

- **[OIII]λ5007/Hβ**. This coefficient is extensively used for studying gas excitation, indicating higher excitation in ionized gas regions where its value is greater. In the map, it is clearly visible that the nodes exhibit higher gas excitation than the internodal region. And if we pay attention to the dark contour of the regions, it coincides with the areas of higher electron density in the previous map.

- **Hγ/Hβ** ratio is useful to trace dust extinction. Both lines are part of the Balmer series, and the value of their ratio is known theoretically (Cardelli et al. 1989). Since dust extinction affects shorter wavelengths more, the intensity of the Hγ will be more affected than Hβ. For recombination case B, T=10000K and n_e=10^2 cm^{-3}, the ratio $j_{H\gamma}/j_{H\beta} = 0.468$ (Osterbrock), and its decimal logarithm is -0.33. The Hγ/Hβ line ratio map for SBS 0335 − 052 W shows a similar value in most spaxels, confirming the low extinction we expected for the galaxy.

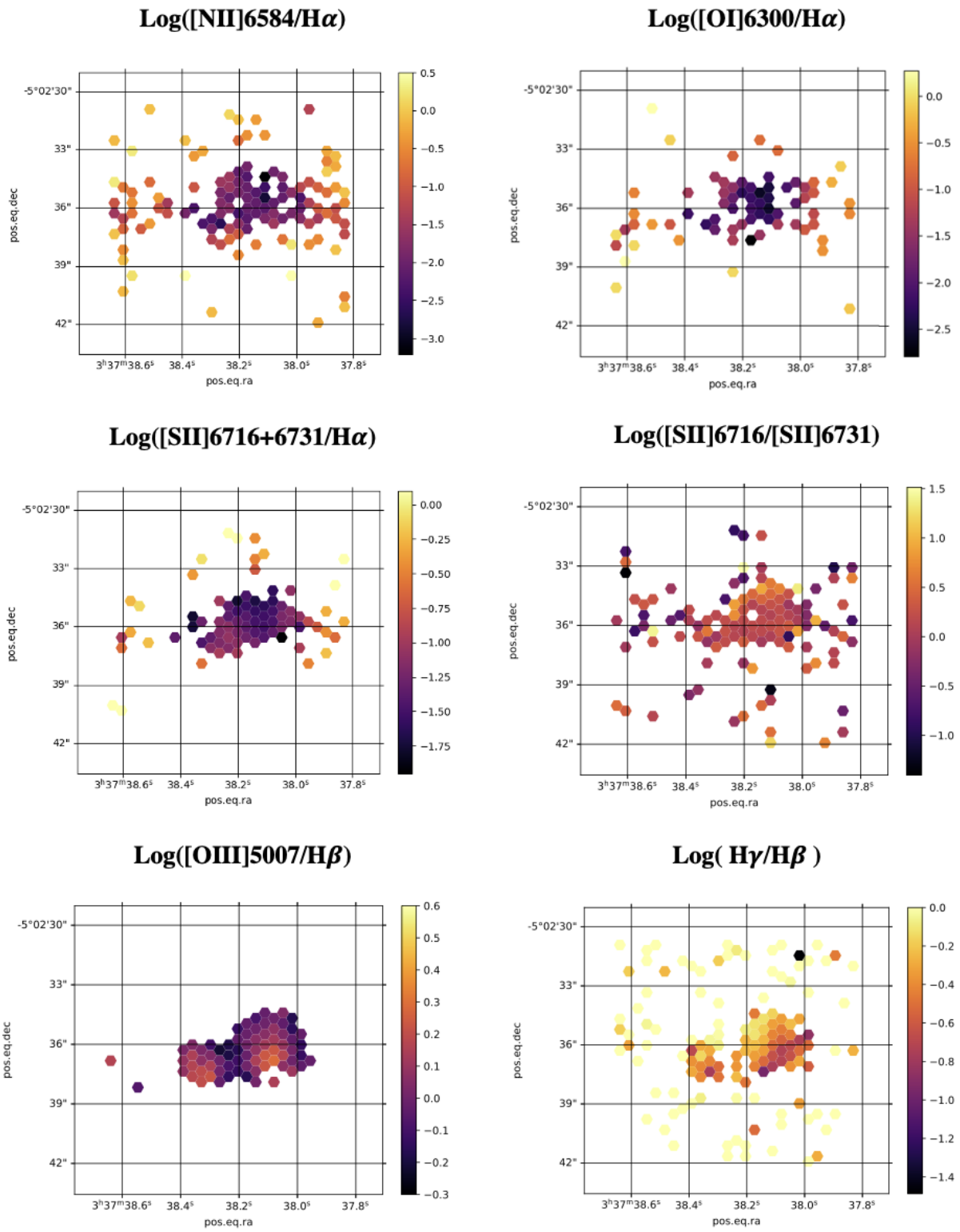


Figure 13: Line ratios of SBS 0335 − 052 W for studying gas ionization, excitation and dust extinction.

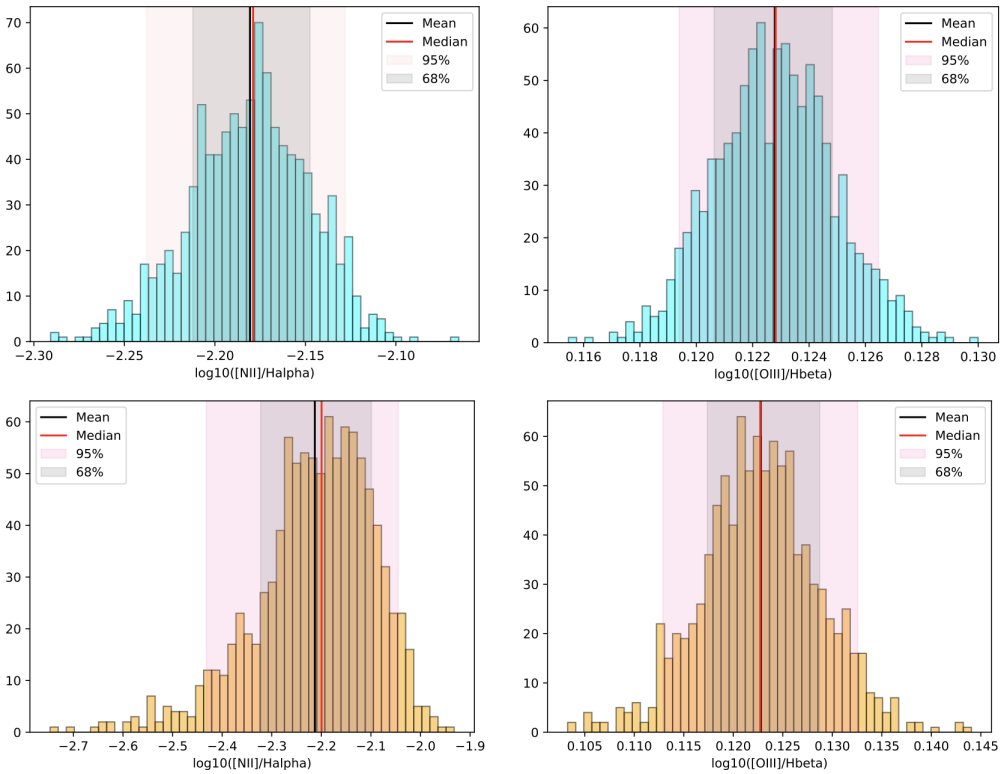


Figure 14: Histograms of the distribution of line ratios obtained from the 1000 simulated spectra generated by including Gaussian noise in the original data (see text for details). Upper row belongs to Region 1 (blue) and lower row to Region 2 (orange).

	$\log([\text{NII}]\lambda6584/\text{H}\alpha)$	$\log([\text{OIII}]\lambda5007/\text{H}\beta)$
$\pm1\sigma$	$-2.181\ ^{+0.034}_{-0.031}$	$0.1223\ ^{+0.0025}_{-0.0570}$
$\pm2\sigma$	$-2.181\ ^{+0.053}_{-0.057}$	$0.1236\ ^{+0.0029}_{-0.0042}$

Table 3: Results of line ratios from Region 1 of SBS $0335-052$ W.

	$\log([\text{NII}]\lambda6584/\text{H}\alpha)$	$\log([\text{OIII}]\lambda5007/\text{H}\beta)$
$\pm1\sigma$	$-2.197\ ^{+0.098}_{-0.130}$	$0.1236\ ^{+0.0052}_{-0.0062}$
$\pm2\sigma$	$-2.20\ ^{+0.15}_{-0.23}$	$0.1236\ ^{+0.0090}_{-0.0110}$

Table 4: Results of line ratios from Region 2 of SBS $0335-052$ W.

4.4. BPT diagram

The Baldwin, Philips and Terlevich diagram (BPT, Baldwin et al. (1981)) allows us to classify galaxies according to the dominant source of ionization radiation. It is a diagram of ratios $[\text{OIII}]\lambda5007/\text{H}\beta$ versus $[\text{NII}]\lambda6584/\text{H}\alpha$. As previously mentioned, $[\text{OIII}]\lambda5007/\text{H}\beta$ provides information about the degree of ionization of the gas, while $[\text{NII}]\lambda6584/\text{H}\alpha$ indicates the radiation hardness. Therefore, if the ionization is produced by an AGN, the galaxy will be located in the right-hand region of the diagram; but if it is due to star formation, it will be found at low values of $[\text{NII}]\lambda6584/\text{H}\alpha$.

For our BPT diagram, we will study the two nodes of SBS $0335-052$ W separately to understand any differences between them, if present. First, spaxel regions over each node have been selected (see figure 12). Since the telescope pointings are not perfectly aligned for the two VPHs, these regions are large enough to include similar flux in both cases. Then, we have extracted their 1D spectrum, and spectral lines Hβ, [OIII]λ5007, Hα, and [NII]λ6584 have been fitted with Python (code `BPT_diagram_Spectra_Simulation`) to obtain their flux as Gaussian areas. Finally, the logarithm of

the ratios has been calculated.

The uncertainties of these ratios have been calculated by simulating in Python 1000 spectra generated by adding random Gaussian noise in the original spectra, where the corresponding standard deviation was determined from the emission-free zone nearby to the considered emission lines. This technique of adding Gaussian noise and simulating spectra was implemented by Cabello (2024) in her PhD Thesis when analyzing near-infrared spectra obtained with the instrument EMIR at GTC. For each simulated spectrum, the BPT diagram ratios have been calculated, which can be visualized in the histograms (see Figure 14). The data distribution is not symmetrical, leading to asymmetric error bars. The pink shade covers 95% of the data, and the gray covers 68%. Results are presented in table 3 and 4 for Regions 1 and 2 respectively, and are represented in figure 15.

Upon examination of the BPT diagram, our calculated ratios lie on the galaxy SBS 0335 − 052 W presented by Izotov et al. (2012), and we conclude that there are not any differences in the ionization mechanisms of both nodes, which overlap on the graph.

4.5. 12 + log(O/H) metallicity

As the final result of the study of the ionized gas in the galaxy SBS 0335 − 052 W, we aim at measuring its metallicity using the N2 and O3N2 tracers. Both are empirical methods for measuring oxygen abundance in HII regions and are widely used for low and high redshift because (1) 'O3N2 is weakly affected by differential extinction and makes use of the strongest and most easily accessible emission lines in the rest-frame optical spectroscopy and (2) N2 uses two emission lines that are very close in wavelength and are also accessible in the near-infrared at moderate-to-high redshifts' (Marino et al. 2013).

The most popular equations for these tracers were presented by Pettini & Pagel (2004) (commonly called PP04). We will use their equations in this study (see Eq. 2 and Eq. 3).

4.5.1. The N2 index

Pettini & Pagel (2004) indicates that the N2 index is particularly useful in low-mass galaxies because 'as (O/H) decreases below solar, there is a tendency for the ionization to increase', so it will be suitable for SBS 0335 − 052 W.

Making use of Eq. (2) from PP04, namely

$$12 + \log(\mathrm{O/H}) = 9.37 + 2.03 \times \mathrm{N2} + 1.26 \times \mathrm{N2}^2 + 0.32 \times \mathrm{N2}^3, \tag{2}$$

we have estimated the metallicity and associated uncertainty for the measured N2 in the MEGARA spectra. The results for Region 1 and 2 are presented in Table 5 and 6, respectively, and displayed in Figure 16.

4.5.2. The O3N2 index

We can also reconsider the case of calculating metallicity using two ratios. Alloin et al. (1979) were the first to introduce index O3N2. Marino et al. (2013) expected the 'inclusion of [OIII]5007 to be most useful in the high metallicity regime where [NII] saturates but the strength of [OIII]5007 continues to decrease with increasing metallicity'. Using equation

$$12 + \log(\mathrm{O/H}) = 8.73 - 0.32 \times \mathrm{O3N2}, \tag{3}$$

which is Eq. 3 from PP04, we have calculated the oxygen abundance with index O3N2 and it is presented in figure 17, where the underlying image belongs to Marino et al. (2013) study.

Our results are higher than those presented by Izotov et al. (2009) (Table 1) for both regions and for both tracers. The measurements are not compatible considering the uncertainty intervals. Specifically, the method of estimating oxygen abundance with O3N2 provides the values that deviate the most compared to Izotov et al. (2009). For Region 1, the deviation is 3.4% with N2 and 10% with O3N2. Similarly, for Region 2, the values deviate by 6.1% with N2 and 13% with O3N2. Among

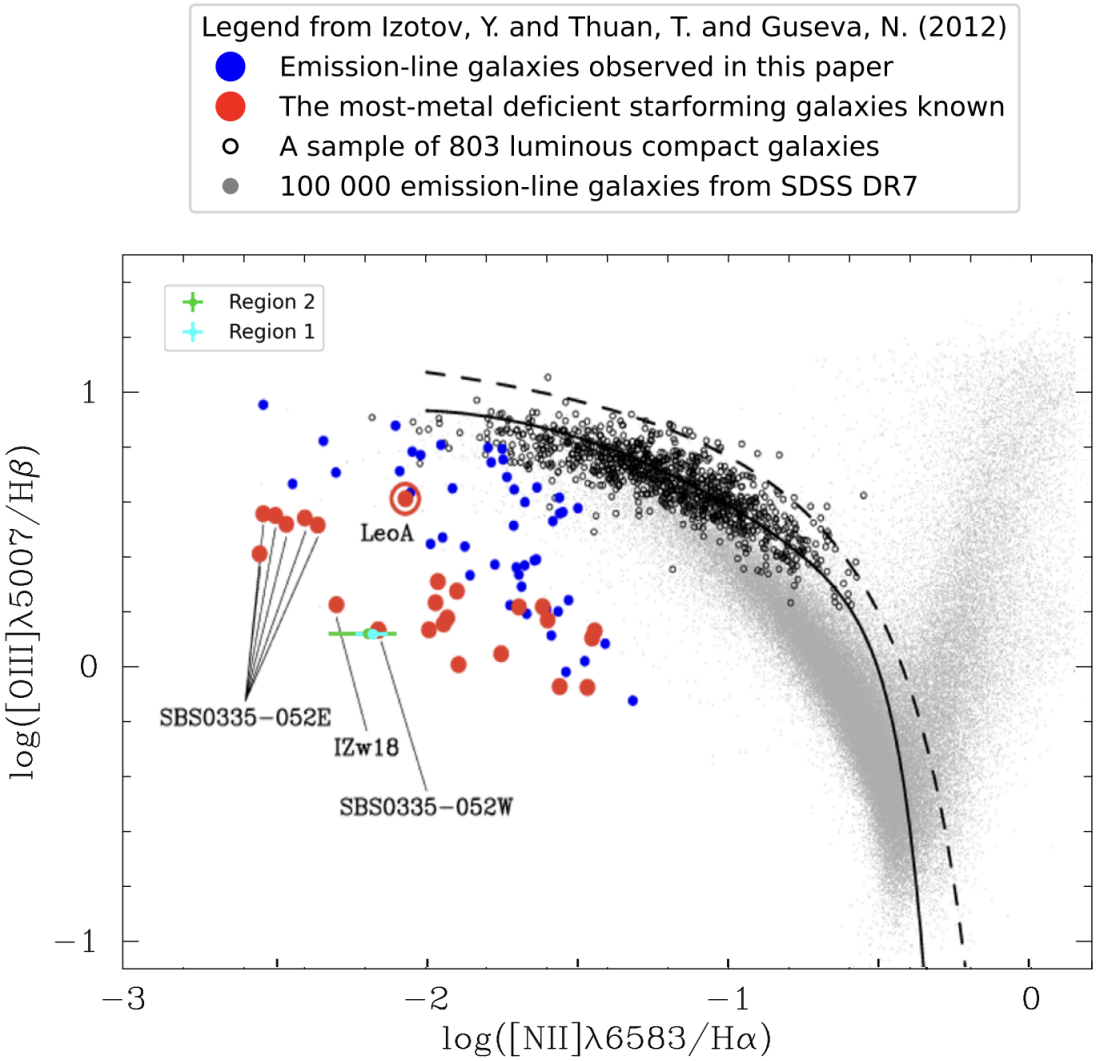


Figure 15: BPT diagram corresponding to Figure 6 from Izotov et al. (2012), where the location of the emission-line galaxies analyzed in that work is shown. The upper legend describes the data represented with red, blue, black and gray symbols. In addition, we overplot the two data points corresponding to the line ratios of Region 1 and 2 in our work (green and cyan symbols, as described in the inner legend). Note that our two data points are almost coincident, specially in the [OIII]5007/Hβ ratio. In addition, our results for the two regions in SBS 0335−052W agree quite well with the average ratio measured by Izotov et al. (2012) for this object.

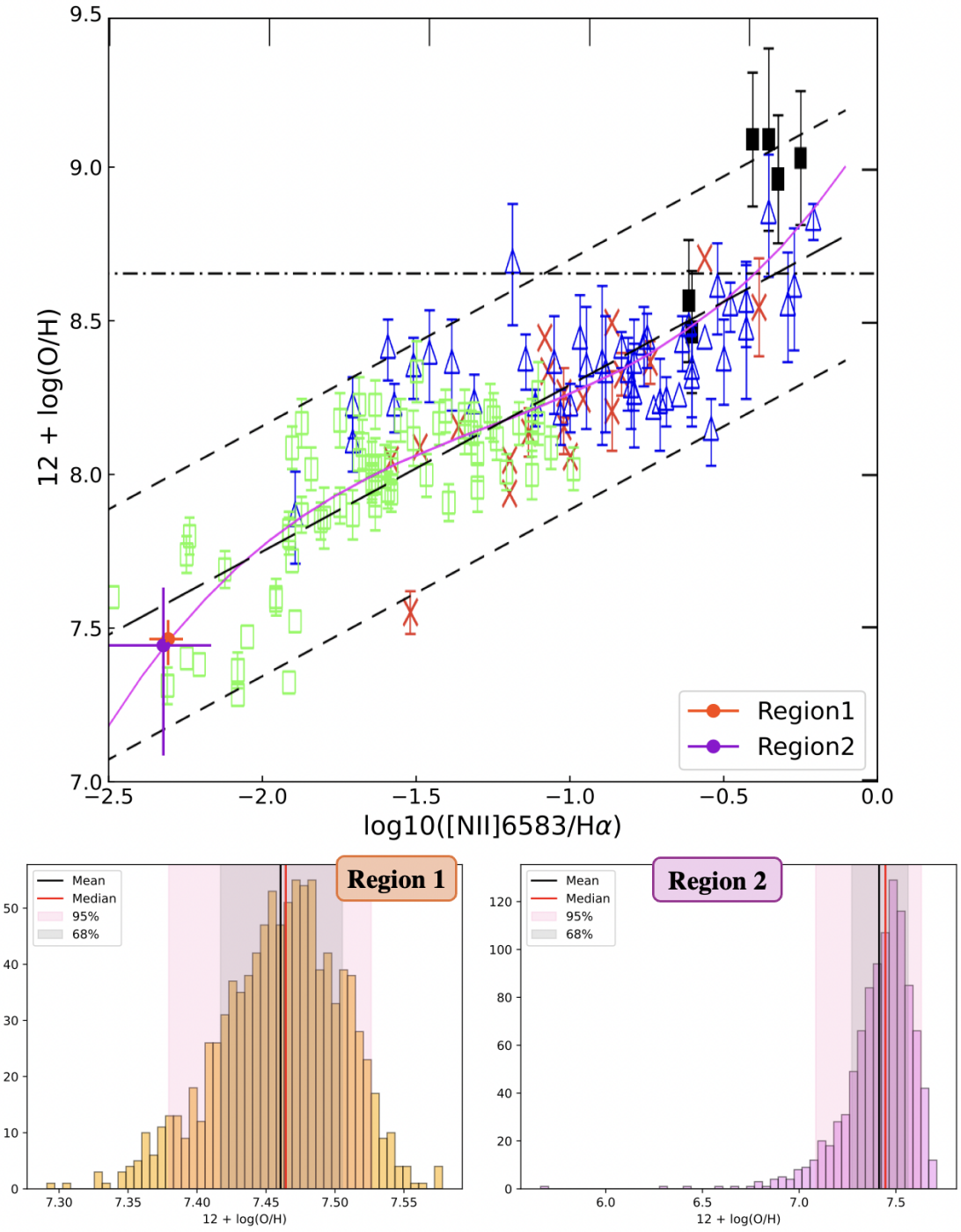


Figure 16: Oxygen abundance against the N2 index in extragalactic H II regions from Pettini & Pagel (2004). Values from Regions 1 and 2 of SBS 0335 − 052 W have been added with their uncertainties. The lower row shows histograms with the distribution of 12+log(O/H) obtained from simulations to provide measurements with errorbars.(Complete legend of symbols 'Filled squares – (O/H) from photoionization models by Díaz et al. (1991 – M 51) and Castellanos, Díaz & Terlevich (2002a,b – NGC 925 and NGC 1637). Crosses – M 101 (Kennicutt, Bresolin & Garnett 2003). Open triangles – spiral and irregular galaxies (Castellanos, Díaz & Terlevich 2002a; Garnett et al. 1997; Gonzalez-Delgado et al. 1994, 1995; Kobulnicky & Skillman 1996; Mathis, Chu & Peterson 1985; Pagel, Edmunds & Smith 1980; Pastoriza et al. 1993; Shaver et al. 1983 [30 Dorand NGC 346]; Skillman et al. 2003; Vílchez et al. 1988). Open squares – blue compact galaxies (Campbell, Terlevich & Melnick 1986; Garnett 1990; Izotov, Thuan & Lipovetsky 1994; Kniazev et al. 2000; Kunth & Joubert 1985; Pagel et al. 1992; Skillman & Kennicutt 1993; Skillman et al. 1994; Thuan, Izotov & Lipovetsky 1995; van Zee 2000; Walsh & Roy 1989). The long-dashed line is the best-fitting linear relationship. The short-dashed lines encompass 95 per cent of the measurements. The solid line is a cubic function'). See Pettini & Pagel (2004) for a complete description of the references listed here.

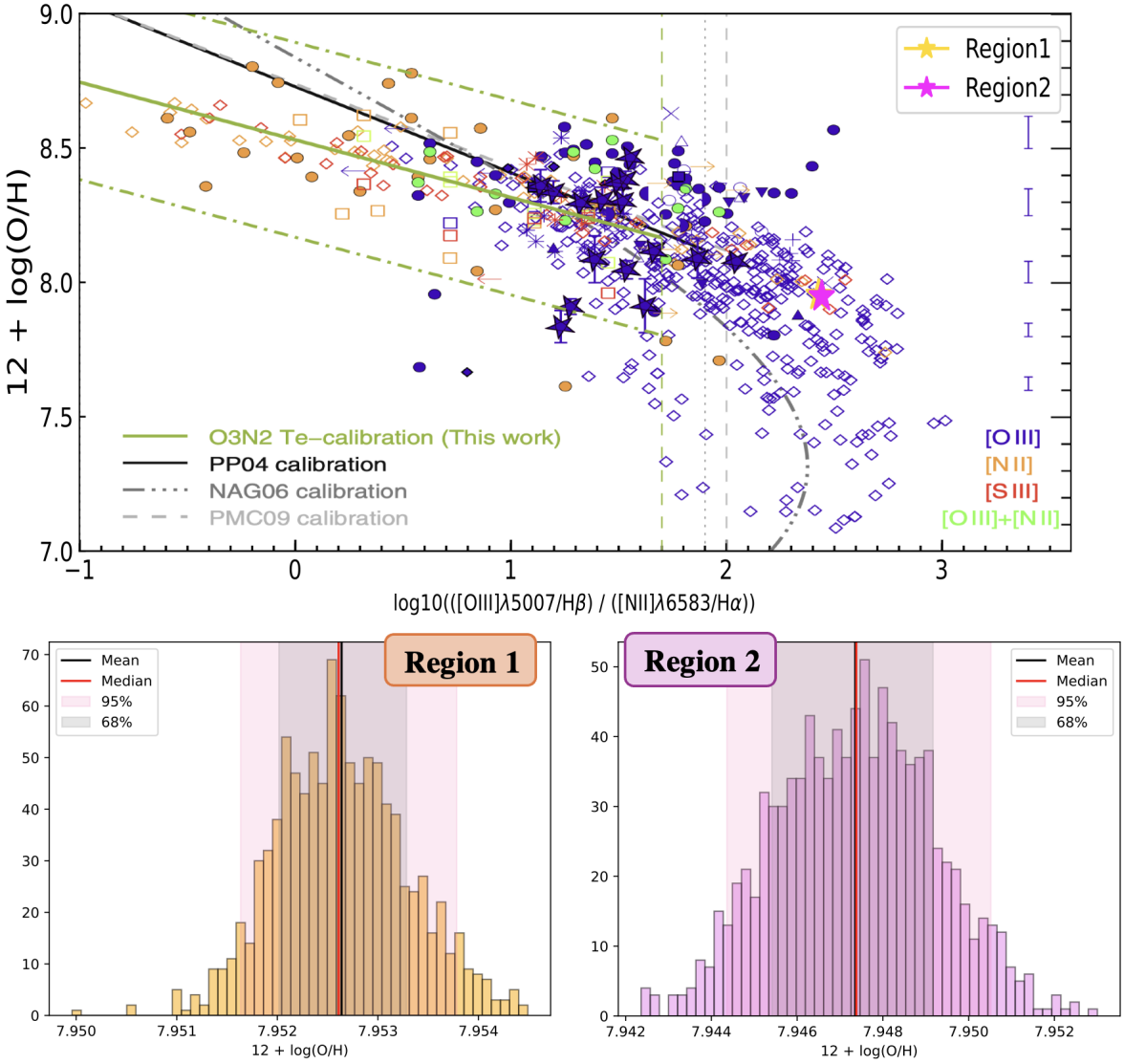


Figure 17: Oxygen abundance against the O3N2 index in extragalactic H II regions from Marino et al. (2013). Values from Regions 1 and 2 of SBS 0335 − 052 W have been added with their uncertainties. The lower row shows histograms with the distribution of 12+log(O/H) obtained from simulations to provide measurements with errorbars. (Complete lengend of symbols: 'filled squares for Berg et al. (2012) data, empty circles for Bresolin et al. (2012) data, filled stars for the new CALIFA-Te data, plus signs for Crowther & Bibby (2009) data, empty upside-down triangles for Croxall et al. (2009) data, filled triangles for Guseva et al. (2012) data, filled upside-down triangles for Hadfield & Crowther (2007) data, crosses for Kehrig et al. (2011) data, filled circles for Pérez-Montero & Contini (2009) data, empty diamonds for Pilyugin et al. (2012) data, filled diamonds for Sanders et al. (2012) data, asterisks for Stasinska et al.(2013) data, empty triangles for Zahid & Bresolin (2011) data, empty squares for Zurita & Bresolin (2012) data, left pointing arrows for GarcíaBenito et al. (2010) data, right pointing arrows for Westmoquette et al. (2013) data, filled left semi-circles for Esteban et al. (2013) data and filled right semi-circles for Monreal-Ibero et al. (2012) data. In blue we show those regions for which the temperature t3,O was computed using the [O III]4363 line; in orange those regions for which we obtain the temperature t2,N from the [NII]5755 line; in red we represent those regions for which we are able to compute the temperature t3,S using the [SIII]6312, and in green are shown those regions that have both [OIII]4363 and [NII]5755 measurements, so we could compute the abundance using t3,O and t2,N. The PP04 calibration is plotted with a black solid line with its applicability interval (from 1 to 1.9) shown with the vertical gray dotted lines. The PMC09 calibration is represented with a gray dashed line until its limit of validity O3N2 = 2. The gray 3-dot-dashed line shows the NAG06 calibration. The new Te-based calibration is shown with a green solid line. The green dot-dashed lines encompass 2 (=±0.36 dex) of all measurements. The vertical dashed lines indicate the interval of Marino et al. (2013) fit, from O3N2 = 1.1 to 1.7.'). See Marino et al. (2013) for a complete description of the references listed here.

	12 + log(O/H) (N2)	12 + log(O/H) (O3N2)
$\pm1\sigma$	$7.464^{+0.041}_{-0.047}$	$7.95263^{+0.00066}_{-0.00061}$
$\pm2\sigma$	$7.464^{+0.062}_{-0.085}$	$7.95263^{+0.00115}_{-0.00099}$

Table 5: Results of 12+log(O/H) of Region 1 of SBS 0335 − 052 W.

	12 + log(O/H) (N2)	12 + log(O/H) (O3N2)
$\pm1\sigma$	$7.44^{+0.12}_{-0.17}$	$7.9480^{+0.0012}_{-0.0025}$
$\pm2\sigma$	$7.44^{+0.19}_{-0.36}$	$7.9480^{+0.0026}_{-0.0036}$

Table 6: Results of 12+log(O/H) of Region 2 of SBS 0335 − 052 W.

the possible reasons that may be influencing this discrepancy in values we could think of influence of cosmic rays, differences in the regions of the galaxy being studied by us and those studied by Izotov et al. (2009), or variations in calibration. However, it is important to remember that we are using metallicity estimators which provide indicative values, but do not represent a precise and complex calculation of metallicity.

Nevertheless, the obtained metallicity values confirm that the galaxy SBS 0335 − 052 W is one of the least metallic in the local universe. For example, the metallicity range associated with Green Peas, which are low-mass galaxies with high star formation, is 12 + log(O/H) = 7.6 to 8.4, and they rarely drop below 12 + log(O/H) = 7.6 (Amorín et al. (2010), Herenz et al. (2023)).

5. Summary and conclusions

The unique study of galaxy SBS 0335 − 052 W using 2D spectroscopy data from MEGARA has provided us with further insights into the galaxy candidate with the lowest measured metallicity to date. From this analysis, the following conclusions and summary have been drawn:

1. Data reduction was performed for two VPHs: LR-B and LR-R, yielding images that required a manual and refined correction for cosmic rays. We have identified many aspects for review and improvement. Firstly, from the MEGARA DRP, we realized the need for an automated intermediate step for cosmic rays removal, as many residual cosmic rays persist in our galaxy. We also noticed the blurring of fibers in the upper right corner of the detector, leading to the development of a new tool for manual fiber tracing. Secondly, related to megaratools, the modification in the code to adjust the plot size to the total field of view of the galaxy, and the numerical issue in velocity calculations.

2. The identification of spectral lines allows us to estimate redshift. For LR-B, its mean is 0.013353 and its standard deviation 0.000010. And for the LR-R, the mean redshift is 0.013379 with a standard deviation of 0.000023, consistent with the tabulated value, and their absolute difference of the means divided by the quadratic sum of the standard deviations results in 1.04 times sigma, so they are also consistent between them. The spectrum exhibits intense emission lines characteristic of galaxies with high star formation and gas ionization.

3. The flux maps provide information about the spatial structure of the galaxy, consisting of two nodes, with Region 1 being more intense in all the analyzed emission lines. On the other hand, the velocity and velocity dispersion maps do not reveal any rotational motion of the galaxy. However, there is a noticeable difference between the areas around the nodes, with lower velocities observed between them compared to the emission regions.

4. As for nodes 3 and 4 that Izotov et al. (2009) detected, we do not observe them because the seeing on the night of observation (0.8”/0.9”) is greater than the spaxel size (0.62”), causing the signal to spread out and blur.

5. The analysis of line ratios (N2 $\equiv$ [NII]λ6584/Hα, [OI]λ3600/Hα, [SII]λ6716+6731/Hα, [OIII]λ5007 /Hβ and Hγ/Hβ) has revealed that this galaxy exhibits areas of low metallicity, high gas excitation and low extinction, particularly around the nodes.

6. In the BPT diagram, it falls within the star-forming ionization zone, and also the value calculated by our study aligns with that of Izotov et al. (2012). Our values, with a 1σ uncertainty, are: for Region 1, log([NII]λ6584/Hα)= $-2.181^{+0.034}_{-0.031}$ and log([OIII]λ5007/Hβ)= $0.1223^{+0.0025}_{-0.0570}$; for Region 2, log([NII]λ6584/Hα)= $-2.197^{+0.098}_{-0.130}$ and log([OIII]λ5007/Hβ)= $0.1236^{+0.0052}_{-0.0620}$.

7. We have corroborated the low oxygen abundance in both nodes using the N2 and O3N2 diagnostics of PP04. For Region 1 (and 1σ uncertainties), 12+log(O/H)=$7.464^{+0.041}_{-0.047}$ (N2) and 12+log(O/H)=$7.95263^{+0.00066}_{-0.00061}$ (O3N2). For Region 2, 12+log(O/H) = $7.44^{+0.12}_{-0.17}$ (N2) and 12 + log(O/H)=$7.9480^{+0.0012}_{-0.0025}$ (O3N2). The results have been higher than those of Izotov et al. (2009), and the O3N2 index introduces greater differences.

As an evolutionary scenario for the SBS 0335−052 galaxy system and the spiral NGC 1376, located at 150 kpc, we could consider the following possibilities: (1) Both SBS galaxies have undergone flybys around NGC 1376 as independent objects, triggering star formation in them, but not synchronously. This could explain why SBS 0335 − 052 W is less metallic, as its star formation occurred later. (2) NGC 1376 may have triggered star formation in the HI cloud where the galaxies are embedded, and they might be undergoing a minor merger. (3) The SBS system may have been a single galaxy initially, which then fragmented into E and W when passing close to NGC 1376. In any scenario, star formation would not have begun simultaneously in SBS 0335 − 052 E and W.

The studies on low-mass local galaxies analogous to the epoch of reionization, which is the focus of the ITP Dwarfs4MOSAIC, will continue to provide more information about their gas properties, kinematics, and evolutionary scenarios, giving us further insights into the birth of the first galaxies in the Universe. Undoubtedly, SBS 0335−052W plays a crucial role in these studies and will continue to be the focus of many future investigations.

6. Future work

The study that we present about SBS 0335 − 052 W opens the doors to future, more detailed research. As first steps, we could implement the automated cosmic ray correction method suggested in this study, since cosmic ray correction in the MEGARA DRP does not seem to be enough, as well as manual fiber tracing using the new megaratools tool. Additionally, observations with another VPH could be done, providing information on the bluer lines.

Regarding uncertainties, what we have presented in this study is a simplified method of adding Gaussian noise to a one-dimensional spectrum. In future projects, we could simulate two-dimensional images and make them undergo the MEGARA reduction pipeline for uncertainty calculations.

Indeed, the galaxy SBS 0335 − 052 W is one of the galaxies with the lowest metallicity found to date. In this study, we have only examined the properties of the ionized gas, but we have not taken into account the presence of an underlying stellar population, which will be considered in future work, along with other techniques and more VPHs.

References

Alloin, D., Collin-Souffrin, S., Joly, M., & Vigroux, L. 1979, Astronomy and Astrophysics, vol. 78, no. 2, Sept. 1979, p. 200-216., 78, 200

Amorín, R. O., Pérez-Montero, E., & Vílchez, J. 2010, The Astrophysical Journal Letters, 715, L128

Arroyo-Polonio, A., Iglesias-Páramo, J., Kehrig, C., et al. 2023, Astronomy & Astrophysics, 677, A114

Atek, H., Labbé, I., Furtak, L. J., et al. 2024, Nature, 626, 975

Baldwin, J. A., Phillips, M. M., & Terlevich, R. 1981, Publications of the Astronomical Society of the Pacific, 93, 5

Cabello. 2024, Técnicas experimentales para el estudio de galaxias distantes con instrumentación puntera de GTC, https://hdl.handle.net/20.500.14352/93258

Cardelli, J. A., Clayton, G. C., & Mathis, J. S. 1989, Astrophysical Journal, Part 1 (ISSN 0004-637X), vol. 345, Oct. 1, 1989, p. 245-256., 345, 245

Castillo-Morales. et al. 2020, MEGARA Cookbook, https://zenodo.org/records/3932063#.Y2k2bezMJnw

de Paz, A. G., Madore, B., & Pevunova, O. 2003, The Astrophysical Journal Supplement Series, 147, 29

Ekta, B., Pustilnik, S. A., & Chengalur, J. N. 2009, Monthly Notices of the Royal Astronomical Society, 397, 963

Elmegreen, D. M. & Elmegreen, B. G. 1987, Astrophysical Journal, Part 1 (ISSN 0004-637X), vol. 314, March 1, 1987, p. 3-9., 314, 3

Fan, X., Strauss, M. A., Becker, R. H., et al. 2006, AJ, 132, 117

Filho, M. E., Winkel, B., Sánchez Almeida, J., et al. 2013, , 558, A18

Gil de Paz, A., Carrasco, E., Gallego, J., et al. 2016, in Ground-based and Airborne Instrumentation for Astronomy VI, Vol. 9908, SPIE, 420–439

Gil de Paz, A., Gallego, J., Carrasco, E., et al. 2015, Highlights of Spanish Astrophysics VIII, 804

Herenz, E., Inoue, J., Salas, H., et al. 2023, Astronomy and Astrophysics, 670, A121

Herenz, E. C., Hayes, M., Papaderos, P., et al. 2017, , 606, L11

Izotov, Y., Guseva, N., Fricke, K., & Papaderos, P. 2009, Astronomy & Astrophysics, 503, 61

Izotov, Y., Thuan, T., & Guseva, N. 2012, Astronomy and Astrophysics, 546, 122

Izotov, Y. I., Thuan, T. X., & Guseva, N. G. 2005, The Astrophysical Journal, 632, 210

Izotov, Y. I., Thuan, T. X., & Guseva, N. G. 2024, , 527, 3486

Kimm, T., Katz, H., Haehnelt, M., et al. 2017, Monthly Notices of the Royal Astronomical Society, 466, 4826

Krabbe, A., Hernandez-Jimenez, J., Mendes de Oliveira, C., et al. 2024, Monthly Notices of the Royal Astronomical Society, 528, 1125

Marino, R. A., Rosales-Ortega, F., Sánchez, S., et al. 2013, Astronomy & Astrophysics, 559, A114

Paswan, A., Saha, K., Leitherer, C., & Schaerer, D. 2022, The Astrophysical Journal, 924, 47

Pérez-Montero, E. 2017, Publications of the Astronomical Society of the Pacific, 129, 043001

Pettini, M. & Pagel, B. E. 2004, Monthly Notices of the Royal Astronomical Society, 348, L59

Pustilnik, S., Lipovetsky, V., Izotov, Y. I., et al. 1997, Astronomy Letters

Pustilnik, S. A., Brinks, E., Thuan, T. X., Lipovetsky, V. A., & Izotov, Y. I. 2001, The Astronomical Journal, 121, 1413

Rix, H.-W. & Zaritsky, D. 1995, arXiv preprint astro-ph/9505111

Thompson, R. I., Sauvage, M., Kennicutt, R. C., et al. 2009, The Astrophysical Journal, 691, 1068

Thompson, R. I., Sauvage, M., Kennicutt Jr, R. C., Engelbracht, C. W., & Vanzi, L. 2006, The Astrophysical Journal, 638, 176

Thuan, T. X., Bauer, F. E., Papaderos, P., & Izotov, Y. I. 2004, The Astrophysical Journal, 606, 213

Thuan, T. X., Izotov, Y. I., & Lipovetsky, V. A. 1997, , 477, 661

Wise, J. H. 2019, Contemporary Physics, 60, 145–163

Wofford, A., Vidal-García, A., Feltre, A., et al. 2021, , 500, 2908